Effect of geometrical irregularities on fatigue of lead sheathing for submarine high voltage power cable applications

Edgardo Moreno [a], Luigi Mario Viespoli [b,c,*], Audun Johanson [d], Di Wan [c], Antonio Alvaro [b,c], Aurelio Soma' [a], Filippo Berto [c]

[a] Dipartimento di Ingegneria Meccanica e Aerospaziale, Politecnico di Torino, Italy
[b] Sintef Industry, Richard Birkelands vei 2B, 7031 Trondheim, Norway
[c] Department of Mechanical and Industrial Engineering, Norwegian University of Science and Technology (NTNU), Richard Birkelands vei 2B, 2034 Trondheim, Norway
[d] Nexans Norway, Innspurten 9, 0663 Oslo, Norway

A B S T R A C T

High voltage subsea power cables are typically composed of several layers, including: a conductive core, a dielectric layer, a ductile metallic watertight barrier and a series of radial and axial armours and polymer layers. The watertight barrier serves the purpose of preventing water permeating to the dielectric due to the outer layers' polymer hygroscopicity. Water impregnation may cause dielectric breakdown, with fatal consequences on the integrity of the power cable. The watertight barrier is made of extruded lead alloy and is subjected, during the installation and operational life of the component, to axial and radial displacement-controlled fatigue which might lead to cracking, thus to a loss of its isolating properties. Lead, due to the low melting temperature, is characterized by creep deformation and damage even at room temperature. A steel tape is winded around the polyethylene sheathing surrounding the lead barrier, which is deformed, and a helical ridge is generated. This irregularity causes a local concentration of strain which might potentially lead to early failure of the lead sheathing. In this work the results of displacement-controlled fatigue testing at different strain rates of sheathing material including the irregularity is presented and compared to the results in equivalent conditions, but in the absence of the irregularity. The strain concentration caused by the defect is analysed with the implementation of a creep material model calibrated on the cyclic properties of the alloy and the notch sensitivity of the material for the class of defects, temperature and frequency in exam is obtained. The results are applied to the modelling of the stress-strain field in the component with and without irregularity and conclusions are drawn on the danger that such irregularities pose on the structural integrity on the power cable.

1. Introduction

Subsea high voltage power cables need a watertight sheathing covering the dielectric layer to prevent water from permeating it causing the failure of the powerline for dielectric breakdown. The material used to produce the sheathing must satisfy a series of requirements: it must be chemically stable, not permeable by water, endure the load history of the cable without cracking and it should be easy to extrude. The load history of a power cable is composed of an initial phase of high strains due to the production and installation phases and a subsequent series of smaller deformation cycles due to thermal expansions and, in dynamic applications, wave and tidal motion, which lasts for the operational life of the component, that is around 25 years. The materials traditionally used for such application are lead alloys of various type, according to the specific type of cable and operational conditions. The low melting temperature of lead alloys, around 600 K, causes the activation of time-dependent phenomena at the operational temperature, which corresponds to room temperature or slightly higher. When a metal is

subjected to stress at a temperature sufficient for the activation of diffusive processes, creep occurs. Depending on the conditions and stress applied, this may be dominated by dislocation glide and climb and by diffusional alteration of the grain geometry. When cyclic loading happens at a sufficiently elevated temperature, creep deformation favours the nucleation of fracture, especially at the grain boundary, which are weakened by the high temperature [1]. The propagation of fatigue crack happens also at an increased rate, leading to an overall shorter endurance to cyclic loading when such phenomena are relevant [2]. Creep deformation, creep-fatigue interaction and recrystallization should then be considered in the fatigue analysis of the sheathing. The study of the mechanical performance of lead alloys used by the cable industry is a highly specialized topic of industrial interest, and therefore the literature available on the subject is limited. A substantial part of the research work dealing with the mechanical properties of lead alloys for power cable sheathing was performed between the years 30s and 80s of the past century, exploring the tensile properties at different temperature, the influence of microstructure and thermal treatments and the fatigue performance [3–9].

List of symbols

E	Young's modulus.
ν	Poisson's ratio.
k_ε	Stain concentration factor.
q	Notch Sensitivity.com
k_f	Fatigue concentration factor.
k',n'	Ramberg-Osgood equation parameters.
ε_g	Global strain amplitude.
A, n, m	Power Law Creep parameters.
$\sigma_{eq,d}$	Equivalent deviatoric stress.
$\varepsilon_{eq,cr}$	Equivalent creep strain.
$A_{el},b_{el},A_{pl},b_{pl}$	Coffin-Manson-Basquin parameters.
$\varepsilon_{max,eq}$	Equivalent Von-Mises strain amplitude.
N_s,N_i	Number of cycles to failure for Smooth and Irregular specimens.

This local strain concentration might negatively affect the fatigue life of the sheathing and then pose a threat to the structural integrity of the entire cable.

The present work focuses on the impact of these irregularities on the fatigue life of the lead sheathing subjected to strain control fatigue. Small scale fatigue results are presented at different strain rates with and without irregularities. A creep material model is calibrated on the stabilized cyclic curve of the Pb-Sn-Sb alloy of interest and the two types of specimens are modelled in finite element method. The results in terms of equivalent strain range obtained at the most heavily loaded of the specimen are used to compute the alloy's notch sensitivity for this type of mild notch. To conclude the analysis, a section of the power phase was modelled and the local increment of strain caused by the irregularity was used, together with the notch sensitivity previously computed, to estimate the reduction of fatigue life caused by the presence of the defect. Due to the highly plastic behaviour generated by room temperature creep deformation, lead alloys are characterized by limited notch sensitivity and the reduction of fatigue life in the component is estimate in the order of magnitude of a fifth of the total cycles.
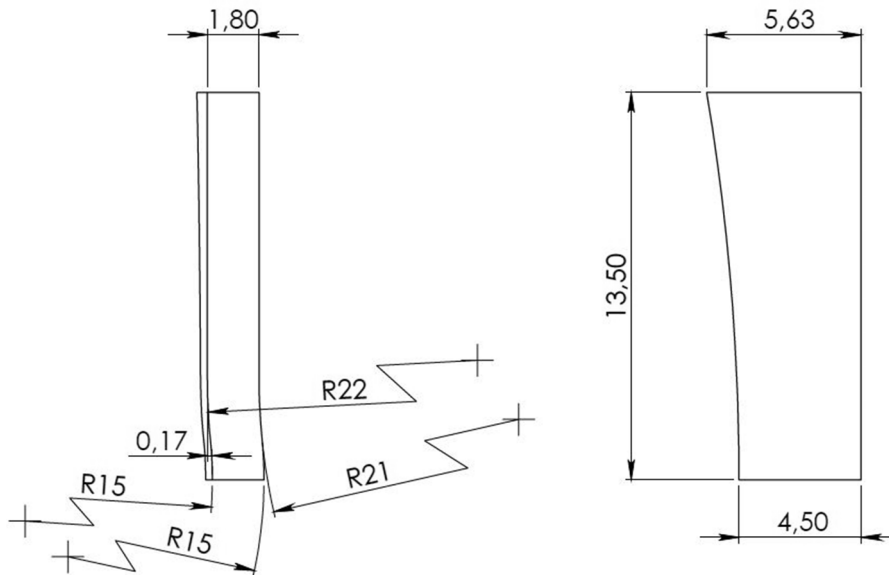

Fig. 1. Geometrical discontinuity on a fourth of the specimen. Clamping area excluded.

A new series of scientific studies has been performed and published in the recent years due to an increased industrial interest in gaining an understanding of the deformation and damage behaviour of the alloys of interest with up-to-date techniques and loading condition of relevant practical interest. The main topics investigated by these more recent research works are: tensile behaviour, with focus on the strain rate sensitivity, and microstructure [10] steady state creep deformation [11] strain control fatigue at specimen scale [12] and full scale [13] and influence of production defects on the fatigue performance [14,15]. The evolution of monotonic and cyclic damage has been observed in-situ [16] and full cable sections have been modelled to understand the influence of design parameters on the component behaviour [17–19].

Mass impregnated subsea power phases include, above the lead and high-density polyethylene sheathings, a layer made of a galvanized steel tape winded in pretension at an angle from the longitudinal direction of about 70°. The purpose of this component of the cable is to contrast the thermal expansion of the dielectric, providing a compressive stress state to the layers underneath. The negative triaxiality originated by this compression is beneficial for the fatigue life of the lead sheathing, as discussed in [19]. The compression caused by the steel tape deforms the layers underneath originating helical grooves on the lead sheathing.

2. Experimental setup

In order to characterize the effect of certain geometrical discontinuities on the lead layer, fatigue axial tests, with a strain ratio $R_\varepsilon = -1$, were performed in strain control, in air and at room temperature on a series of lead E-alloy hourglass-shaped specimens. These were affected in the restricted section by the irregularity shown in Fig. 1. The results of this testing were then compared to the results of fatigue testing on smooth specimens (Fig. 2) available in the literature [12] to quantify the notch sensitivity of the alloy. The *PbSnSb* alloy used in this work is identical, in terms of composition and extrusion conditions, to the alloy tested in [10] *Pb 99.3%, Sn 0.45%* and *Sb 0.25%*. The aforementioned work contains the microstructure investigation of the alloy. Being lead alloys subjected to creep deformation and damage, which is strain-rate sensitive, different strain rates were tested. In particular, the fatigue tests were performed at the nominal strain rates of 1E-2, 1E-3 along the longitudinal direction for the smooth specimens, and for the irregular ones.

From the experimental analysis, data regarding the stabilised hysteresis loop were collected, that is the engineering stress (measured by the load cell on the specimen's restricted section) and the real strain
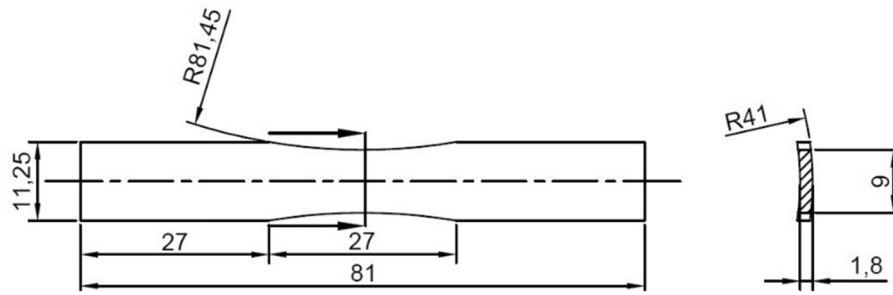
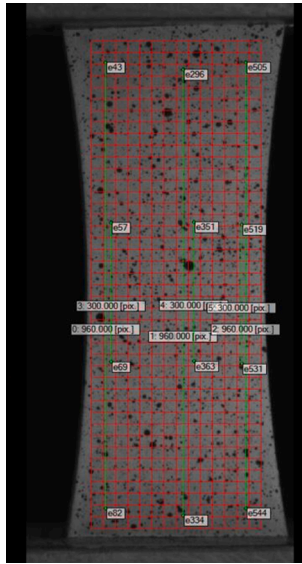**Fig. 2.** . Smooth lead specimen geometry.

Fig. 3. DIC grid and measurement segments (vectors) projected on the specimen's surface. Note the "short" (central) and "long" (full gauge length) vectors.
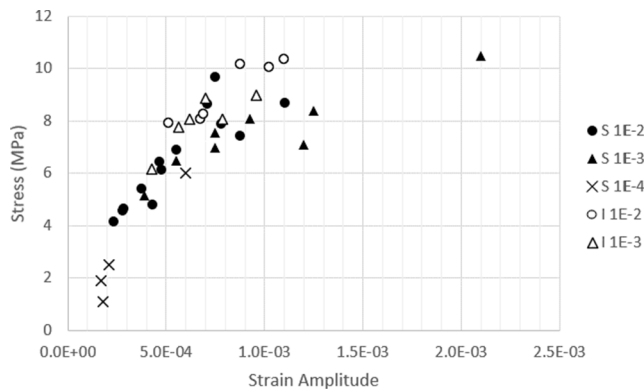

Fig. 4. Stabilised stress and strain amplitude for the smooth (S) and irregular (I) specimens at the tested strain rates.

Fig. 5. Fatigue data for the smooth (S) and irregular (I) specimens at the tested strain rates.

Table 1
Ramberg-Osgood parameters for the best-fitting cyclic curves.

Strain rate (s-1)	$E(GPa)$	$k^{'}$	$n^{'}$
1E-2	15	30	0.162
1E-3	15	20	0.122
1E-4	15	15	0.112

measured near to their centre, on the central vectors shown in Fig. 3. In the second place, the DIC was used on the irregular specimens to measure the strain along the full gauge length vectors in Fig. 3 (since the three-dimensional geometry of the discontinuity led to uncertainty in computing the strain along the "short" segments with bidimensional DIC).

These data were plotted in Fig. 4 and Fig. 5. The experimental data regarding to the 1e-4 strain rate were only available to represent the stabilised cyclic curve, while in the fatigue plots, the empty markers are representing the Run-out conditions.

3. Cyclic curve: material model calibration

In order to model the specimen's behaviour with respect to the strain rate sensitivity of the alloy, the material model calibration was based on the stabilized cyclic behaviour of the smooth specimens, tested at the three strain rates aforementioned. Before calibrating the material creep model in FEM, the cyclic curves for the calibration were obtained from these experimental points. The stress and strain amplitude of the various fatigue tests were interpolated by means of the best-fitting cyclic curves, which shape is described by the Ramberg-Osgood equation (Equation 1 [20]) in all the three different strain rates. Although the elastic modulus of lead is subjected to a certain degree of strain rate sensitivity [10] for simplicity a constant Young modulus' value of $E = 15'000MPa$ was

along the longitudinal direction. This was measured by means of bidimensional Digital Image Correlation (DIC) in the middle of the specimen from the convex side. An example of the speckle pattern, together with the digital grid of linear elements, is plotted in Fig. 3. The vectors used for the measurement of the strain can be seen in the same figure. For vector it is intended the distance between two pixels in the DIC mesh. The measure of the relative displacement between these points corresponds to an average of the strain along the vector's direction.

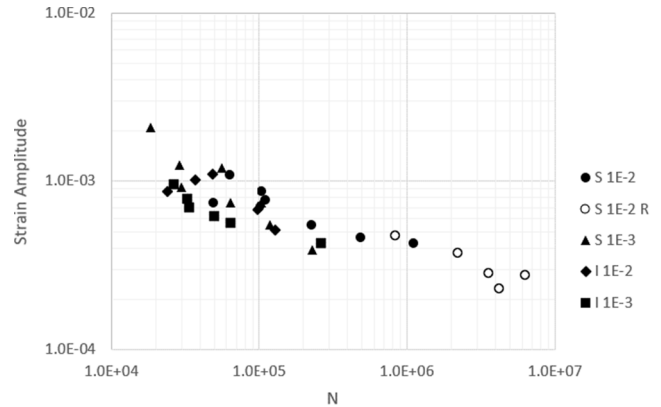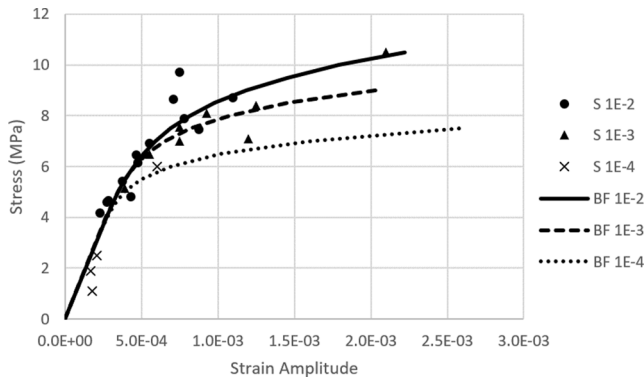Starting from the smooth specimens, the strain amplitude was

Fig. 6. Best Fitting (BF) Cyclic curves for the smooth specimens' tests (S).
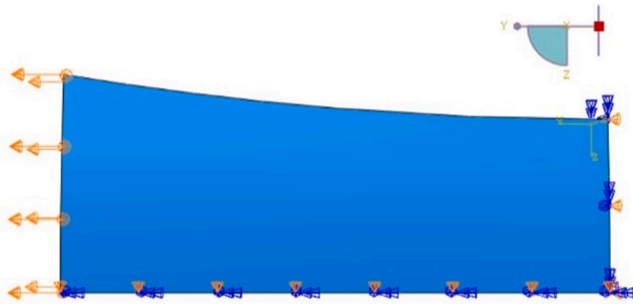

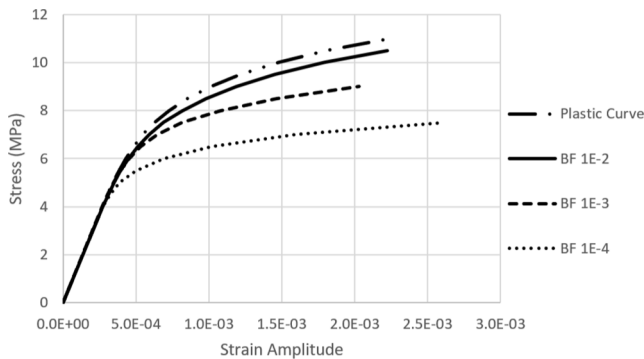**Fig. 7.** Symmetrical boundary conditions and Displacement.

Fig. 8. Plastic curve compared with the cyclic curves.

Table 2
Lead plastic table.

Stress (MPa)	Plastic Strain	Stress (MPa)	Plastic Strain	Stress (MPa)	Plastic Strain
4.16	0.00	7.50	$1.24E-04$	11.00	$1.51E-03$
4.50	$1.87E-06$	8.00	$1.89E-04$	11.50	$2.01E-03$
5.00	$6.40E-06$	8.50	$2.82E-04$	12.00	$2.65E-03$
5.50	$1.42E-05$	9.00	$4.09E-04$	12.50	$3.45E-03$
6.00	$2.71E-05$	9.50	$5.82E-04$	13.00	$4.45E-03$
6.50	$4.73E-05$	10.00	$8.12E-04$	13.50	$5.68E-03$
7.00	$7.82E-05$	10.50	$1.11E-03$	14.00	1

chosen. The Poisson's ratio $\nu = 0.431$ was known [10] and the parameters k' and n' of the Equation 1 were found (Table 1). The best fitting curves are plotted in Fig. 6.
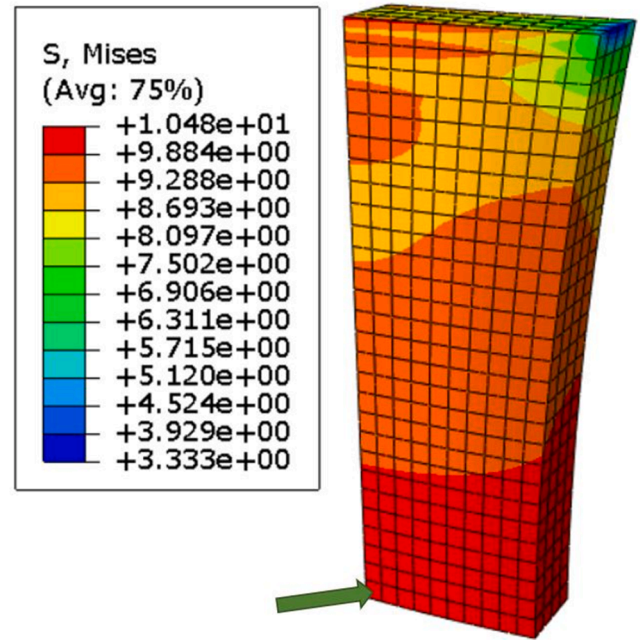
Equation 1 – Ramberg-Osgood equation.

Fig. 9. Element location for the extraction of the outputs for the model calibration.

$$\varepsilon = \frac{\sigma}{E} + \left(\frac{\sigma}{k'}\right)^{\frac{1}{n'}}$$

Once obtained the reference curve for the experimental cyclic behaviour at different strain rates, a creep material model was calibrated comparing the experimental data with the results of three FEM models, one for each strain rate. To reduce the computational time, a fourth of the smooth specimen (without the grabbing parts) was modelled in Abaqus for each strain rate and the best fitting curves were used for the creep parameters calibration. The model is plotted in Fig. 7 with the applied boundary conditions (symmetrical on two faces to reproduce the entire specimen, further than the axial displacement) together with the reference frame.

- The plastic curve was chosen in an arbitrary way with the same shape of the best-fitting curves but shifted at higher stresses to assume that it is exempt from the creep influence (Fig. 8). From this curve, the plastic strain component was extracted and collected in Table 2 together with the correspondent nominal stress.
- Power law creep parameters, in stress-hardening form (being the stress time dependent), which values were computed by an optimization routine implemented in Isight, as discussed in the following. After several iterations using the NCGA optimization algorithm, the optimal power law creep parameters of the Equation 2, which is implemented in Abaqus, were found:
  - A = 3.94e-08.
  - n = 4.218.
  - m = -0.6103.

Equation 2 - Abaqus creep power law, stress-hardening.

$$\dot{\varepsilon}_{eq,cr} = \left(A\sigma_{eq,d}^{n}\left[(m+1)\varepsilon_{eq,cr}\right]^{m}\right)^{\frac{1}{m+1}}$$

The material model calibration required as output from the FEM models the same data collected during the experimental tests. For this reason, the three different testing strain rates were tuned by means of the duration of the displacement along the y direction (Fig. 7). Then, it was created a mesh with quadratic brick elements and the stress and
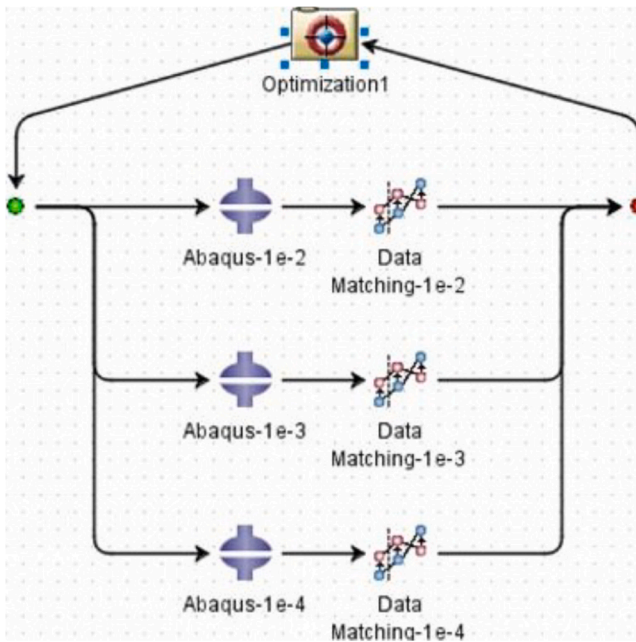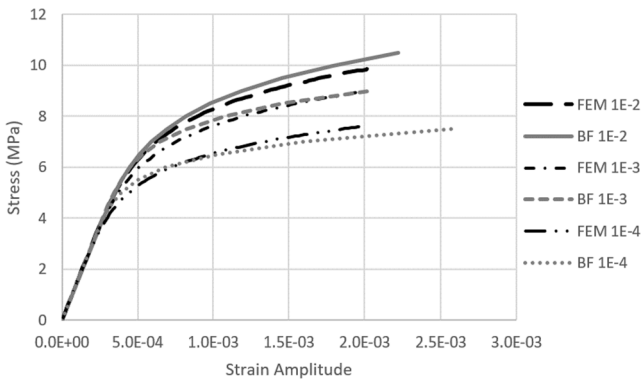
Fig. 10. Isight optimisation layout.

Fig. 11. Comparison between the best fitting (BF) curves and the FEM simulations for the three strain rates.

Fig. 12. Coffin-Manson-Basquin interpolation curves (CMB) for the strain rate 1e-2 s-1 for the smooth data (S 1E-2) and irregular ones (I 1E-2).

strain history output along the y direction (called S22 and E22 respectively) was extracted by the element correspondent to the measurement region on the real specimens (Fig. 9).

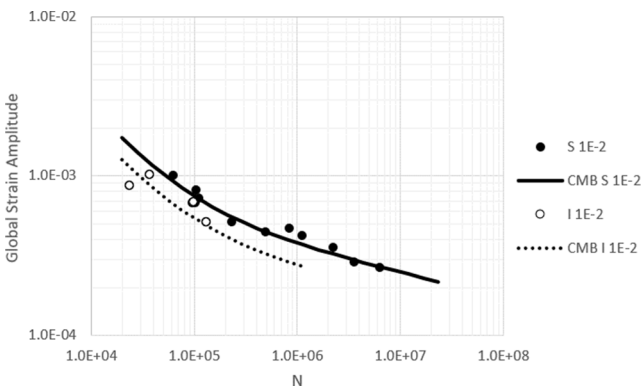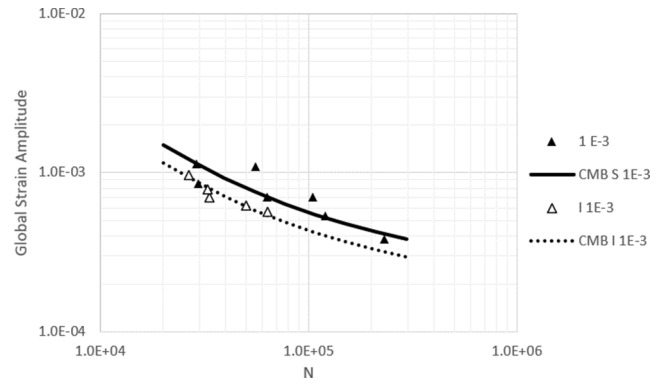On the basis of these outputs, the Isight optimization program

Fig. 13. Coffin-Manson-Basquin interpolation curves (CMB) for the strain rate 1e-3 s-1 for the smooth data (S 1E-2) and irregular ones (I 1E-2).

Table 3
CMB parameters.

Strain rate (1 s-1)	Geometry	A_el	b_el	A_pl	b_pl
1e-2	Smooth	0.0029	−0.153	10.168	−0.922
1e-2	Irregular	0.0021	−0.153	7.4	−0.922
1e-3	Smooth	0.0033	−0.18	85.863	−1.153
1e-3	Irregular	0.0025	−0.18	66	−1.153

(Fig. 10) allowed to compute the optimal creep parameters, which were used as material properties to fit the history output with the best fitting curves of Fig. 6. These creep parameters were considered valid since the maximum error between the simulations and the target curves was less than 10% and the results of the material model calibration is shown in Fig. 11 as a comparison between the best fitting curves and the FEM simulations for the three tested strain rates.

4. Notch sensitivity computation

The experimental results collected for the smooth specimens were then compared to the data coming from the specimens with the irregularity. Since in each tested specimen the irregularity's geometry is slightly different, a mean geometry was sketched and modelled in the restricted section for the simulations (Fig. 1). Then, the calibrated creep parameters, together with the same elastic and plastic material properties were used in these FEM models.

The result of this analysis consists in the notch sensitivity computation (Equation 3), which is given by the fatigue concentration factor k_f and the strain concentration factor k_ε [21].

Equation 3 – Notch sensitivity.

$$q = \frac{k_f - 1}{k_\varepsilon - 1}$$

Due to the distinct plastic behaviour which characterises lead, the fatigue concentration factor (Equation 4) was defined on $\varepsilon_g - N$ fatigue plots, where ε_g is the global strain (thus the strain measured at the specimen extremities) and N is the number of cycles to failure.

Equation 4 - Fatigue concentration factor.

$$k_f = \left(\frac{\varepsilon_{g,smooth}}{\varepsilon_{g,irregular}} \right)_{|N}$$

Thus, considering the experimental data plotted in Fig. 5, their interpolation by means of the Coffin-Manson-Basquin (CMB) equation (Equation 5) allowed to obtain the Fig. 12 and Fig. 13. All the correspondent equation parameters were then collected in Table 3.

Equation 5 - Coffin Manson Basquin equation.

$$\varepsilon_g = A_{el}(N)^{b_{el}} + A_{pl}(N)^{b_{pl}}$$

Table 4
Fatigue notch factors for the tested strain rates.

Strain rate (s-1)	k_f
1E-2	1.37
1E-3	1.30

From these figures is evident that all the data concerning to the irregular specimens are under the data from the smooth ones. It can be deduced that the fatigue life is lower for the irregular specimens, being them subjected to a stress and strain intensification.

Since the experimental data regarding to the irregular specimens are not enough to perform a more precise interpolation, the same slope parameters of the smooth specimen's fatigue curve were used. Therefore, a constant value of k_f was computed for both the strain rates and their values are collected in Table 4.

Then, from the definition of notch sensitivity q (Equation 3), the computation of which is the target of this work, the strain concentration factor k_ε was obtained. Since the fatigue notch factor was computed from the global strain values, rather than the nominal stresses, the *strain concentration factor* was used in the evaluation of the local irregularity's effect (Equation 6).

Equation 6 - Strain concentration factor.

$$k_\varepsilon = \left(\frac{\varepsilon_{max,eq,irr}}{\varepsilon_{max,eq,smo}} \right)_{|\varepsilon_g}$$

The maximum equivalent strain value was found identifying the most solicited point, which corresponds, in both the models, to the external one from the concave side of the restricted section (Fig. 14). This is considered guilty for the fatigue failure for each experimental test and in this point the equivalent Von Mises strain was computed by the Equation 7.

Equation 7 – Equivalent Von Mises strain [22].

$$\varepsilon_{max,eq} = \frac{2}{3} \cdot \sqrt{ \frac{3 \left(e_{xx}^2 + e_{yy}^2 + e_{zz}^2 \right)}{2} + \frac{3 \left(\gamma_{xy}^2 + \gamma_{yz}^2 + \gamma_{zx}^2 \right)}{4} }$$

The equivalent strain values computed along all the simulations were used, together with the global strain, to obtain the $\varepsilon_{max,eq} - \varepsilon_g$ plots,

again, for the strain rates 1E-2 and 1E-3 s-1. An example of the outputs for the higher strain rate is plotted in Fig. 15.

Considering the smooth specimen behaviour as the nominal condition, k_ε was computed at constant global strain (Equation 6). As a result,
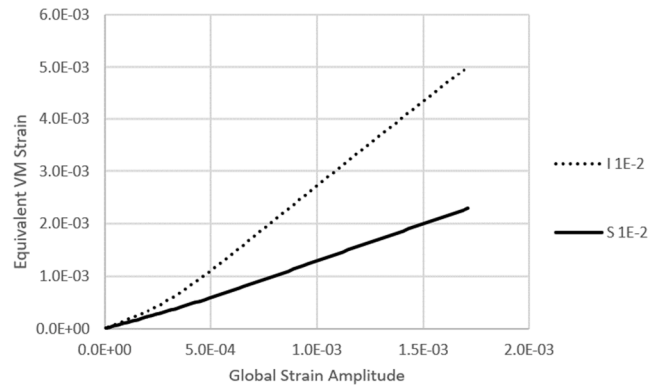
Fig. 15. Strain intensification between the smooth (S) and irregular (I) FEM models for the strain rate 1E-2 s-1.
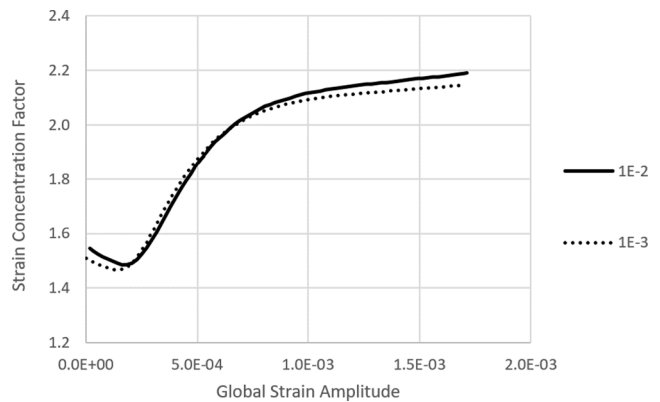
Fig. 16. Strain concentration factor for the two strain rates (s-1).
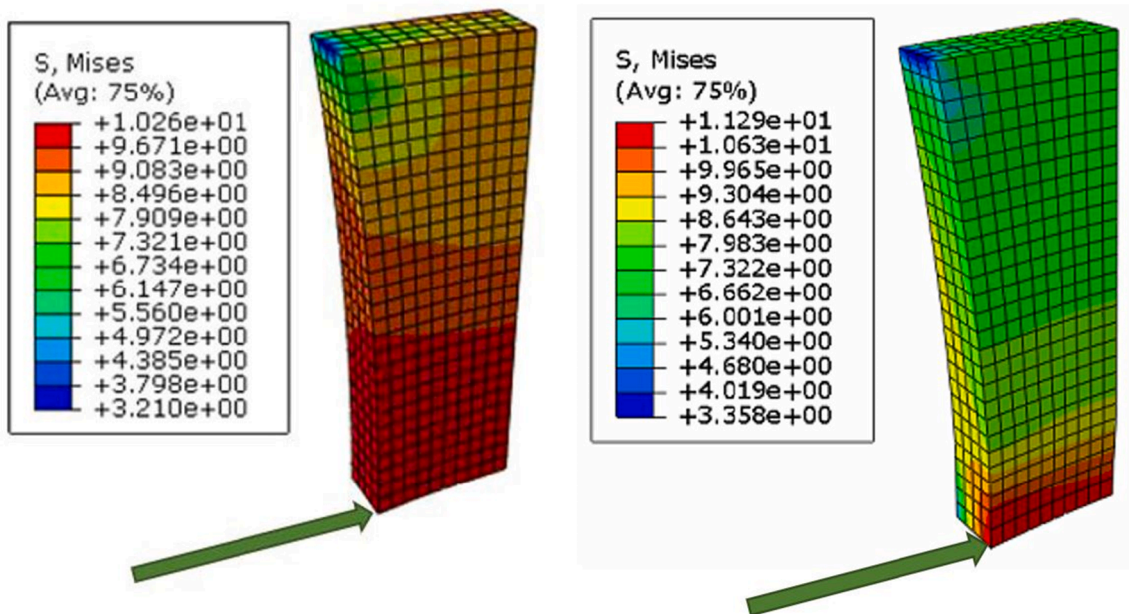
Fig. 14. Most solicited point for smooth (left side) and irregular (right side) models.
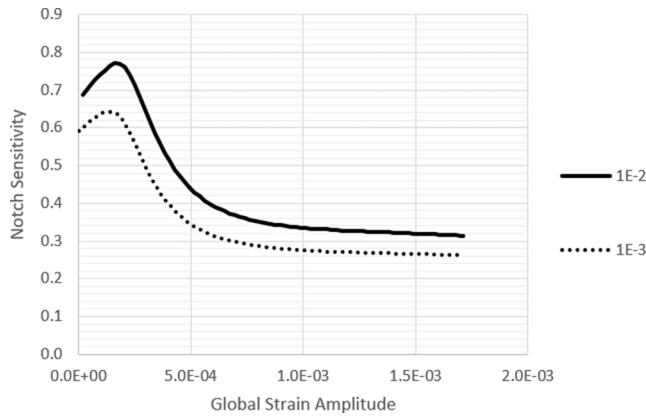
Fig. 17. Notch sensitivity trend for both the strain rates 1e-2 and 1e-3s-1.

Table 5

Notch sensitivity: average values for the two nominal strain rates, global strain amplitude over 5e-4.

Strain rate (s-1)	q
1E-2	0.36
1E-3	0.32

Table 6

Model's cable layers.

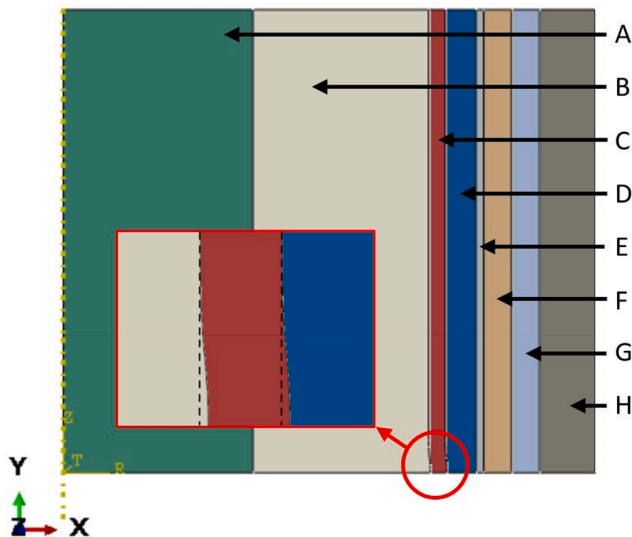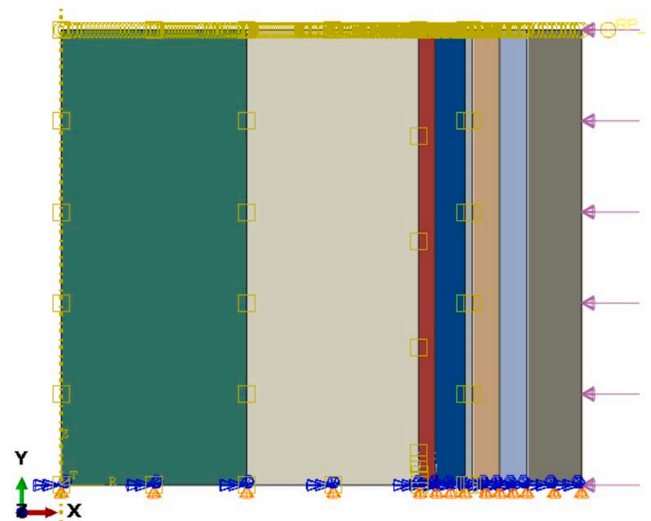| Part	Material	$t(mm)$	$R_{int}(mm)$	$R_{ext}(mm)$
A	Copper Conductor			20.35
B	MI Insulation Paper	18.85	20.35	39.2
C	Lead Sheath	1.8	39.2	41
D	PE Sheath	3.3	41	44.3
E	Steel Tape	0.8	44.3	45.1
F	Steel Armor	3	45.1	48.1
G	Steel Armor	3	48.1	51.1
H	Outer Sheath	6	51.1	57.1

Fig. 18. Cable 2D axisymmetric Model.

Fig. 19. Boundary conditions applied to the 2D axisymmetric models.

the notch strain concentration factor is global-strain dependent and, for the two tested strain rates, the trend shown in Fig. 16 was obtained. In particular, k_t was found to be constant in the elastic field and equal to $k_t \cong 1.5$ for both the strain rates, while in the plastic field it is arising to $k_\varepsilon = 2.2$ for the higher strain rate and $k_\varepsilon = 2.15$ for the strain rate 1E-3 s-1.

Finally, after having computed the fatigue concentration factor and the strain concentration factor, the notch sensitivity could be estimated. This is described by the Equation 3 and in this case it is only global-strain dependent since k_f is constant for these geometries (which are the ones of practical interest). Its trend was plotted in Fig. 17 for both the nominal strain rates.

At the lowest global strains, thus in the elastic field, q is almost constant. At the higher global strains, its value decreases until it stabilises near the values $q = 0.3$ for the highest strain rate and $q = 0.25$ for the strain rate 1E-3 s-1. For the lower strain rate, where the creep phenomenon let the plastic component arising, the notch severity is always lower, and this consideration fits the expectations: materials with a higher plastic behaviour are less damaged by the notch presence.

Finally, to obtain a single value which could be used for design purposes, the average values were computed near the global strain testing conditions and the values in Table 5 were obtained.

5. Component modelling

In the real power cable configuration, the contact between the lead sheathing and the surrounding layers has some effect on the lead sheathing's fatigue resistance. Component fatigue testing has shown how several times the fractures happen at the notch generated by the irregularity on the sheathing. Furthermore, in the real working conditions each layer is subjected to a multiaxial stress field with a high hydrostatic component (rather than the uniaxial stress applied in the experimental tests) which could affect the irregularity influence on the fatigue life of the entire system. To check the response of the lead sheathing in the component, two axisymmetric 2D models (representing a cable's section) were created: the first with an ideal lead sheathing, the second with the geometrical irregularity.

The 2D axisymmetric model was chosen to reduce the computational time. This allowed to produce a refined mesh, which can describe a more accurate stress and strain field in all the cable section and in detail near to the irregularity.

The submarine power cable object of the analysis (Nexans 525 kV Mass-impregnated (MI) HVDC) is made by several layers, but only few of them were modelled being them the most relevant from the structural
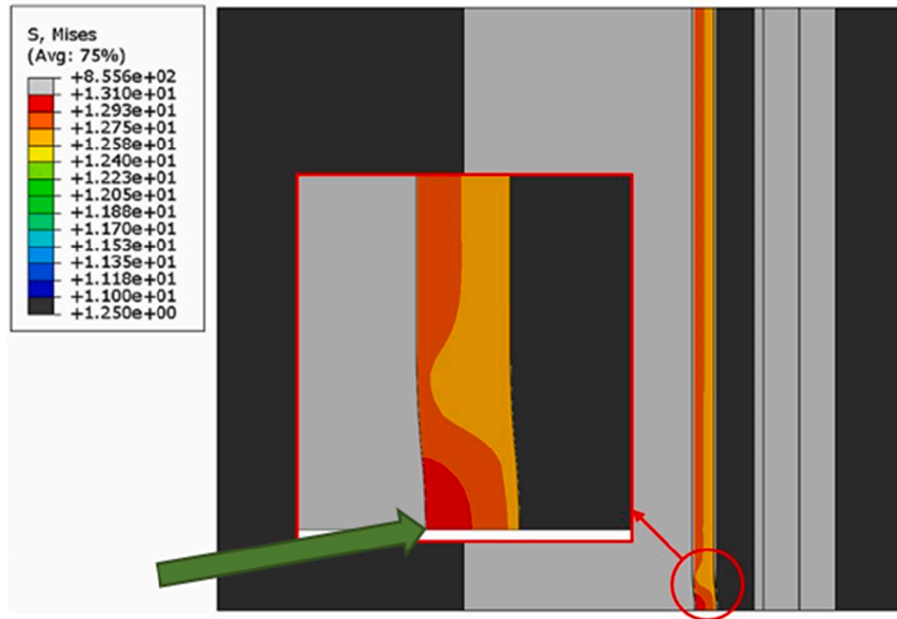
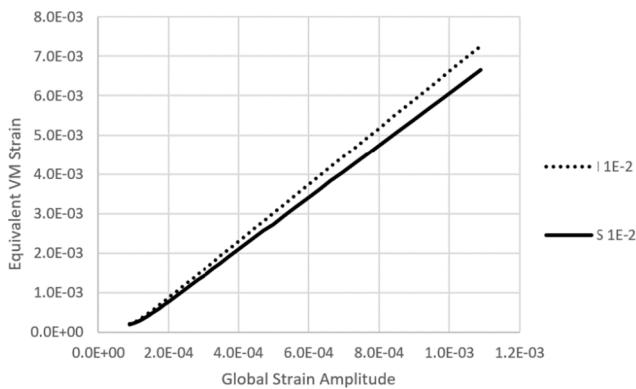**Fig. 20.** Most solicited point of the lead layer.

Fig. 21. Comparison of the Maximum equivalent VM strain between the models with the smooth (S) and irregular (I) lead layer.

Table 7
Strain concentration factors and Fatigue concentration factors for the real power cable configuration.

Strain rate (s-1)	k_ε	k_f
1E-2	1.11	1.041
1E-3	1.11	1.036

Table 8
Percentage life loss for a real power cable.

Strain rate (s-1)	$1 - \dfrac{N_i}{N_{s|pl}}$	$1 - \dfrac{N_i}{N_{s|el}}$
1E-2	4%	23%
1E-3	3%	18%

point of view, in analogy with what done in [19]. Its components are described in Table 6, and they are represented in Fig. 18, where it is highlighted the irregularity geometry, which has the same curvature of the specimens tested (Fig. 1). During the simulations it was

demonstrated that the irregularities have a null or negligible influence on each other and the maximum longitudinal distance at which a noise on the stress field was visible was of about 3*cm*. For this reason, it was created a model with a longitudinal length of 5*cm*. In the end, for sake of simplicity, it was supposed that the geometrical irregularity was entirely absorbed by the surrounding layers, as shown in the magnification of Fig. 18.

To each layer it was assigned their own material properties. These, starting from the elastic properties, the plastic and creep ones, further than the thermal volumetric expansion coefficient α_v were assigned to the correspondent layers and they were taken all from [19]. For the lead sheathing layer were applied the elastic, plastic and creep properties found in the model calibration section of this work.

Then, as shown in Fig. 19:

- A *y-symmetry* boundary condition was adopted on the lower side, to describe the entire irregularity behaviour even if just a half of it was modelled.
- A *periodic* boundary condition was applied on the upper side, to guarantee that each layer could move along the y direction, each with the same longitudinal displacement.
- A contact condition was used between each layer, to guarantee a compatible displacement along the radial direction. In this case, it was chosen to use a Hard contact normal behaviour and a Penalty tangential behaviour. The last boundary condition consists in the water pressure on the external Surface, considering that the cable could be working at about 500*m* depth.

In the real application field, the fatigue cycles to which the cable is subjected are a consequence of different factors (from the cable installation up to the currents forces acting on the cable when it is on the seabed) and in this work only the *thermal cycle* was considered. In detail, the thermal expansion of the inner layers (with a prevalence of the MI paper, which is the layer B in Fig. 18) owing to the Joule effect causes a cyclic plastic deformation of the lead sheathing.

Even if in a more realistic model the temperature gradient should be considered and the expansion of each layer should be studied, in a first approximation the only expansion of the two most internal layers was considered. Indeed, the other layers are subjected to a significant lower temperature gap and their thermal expansion coefficient is negligible
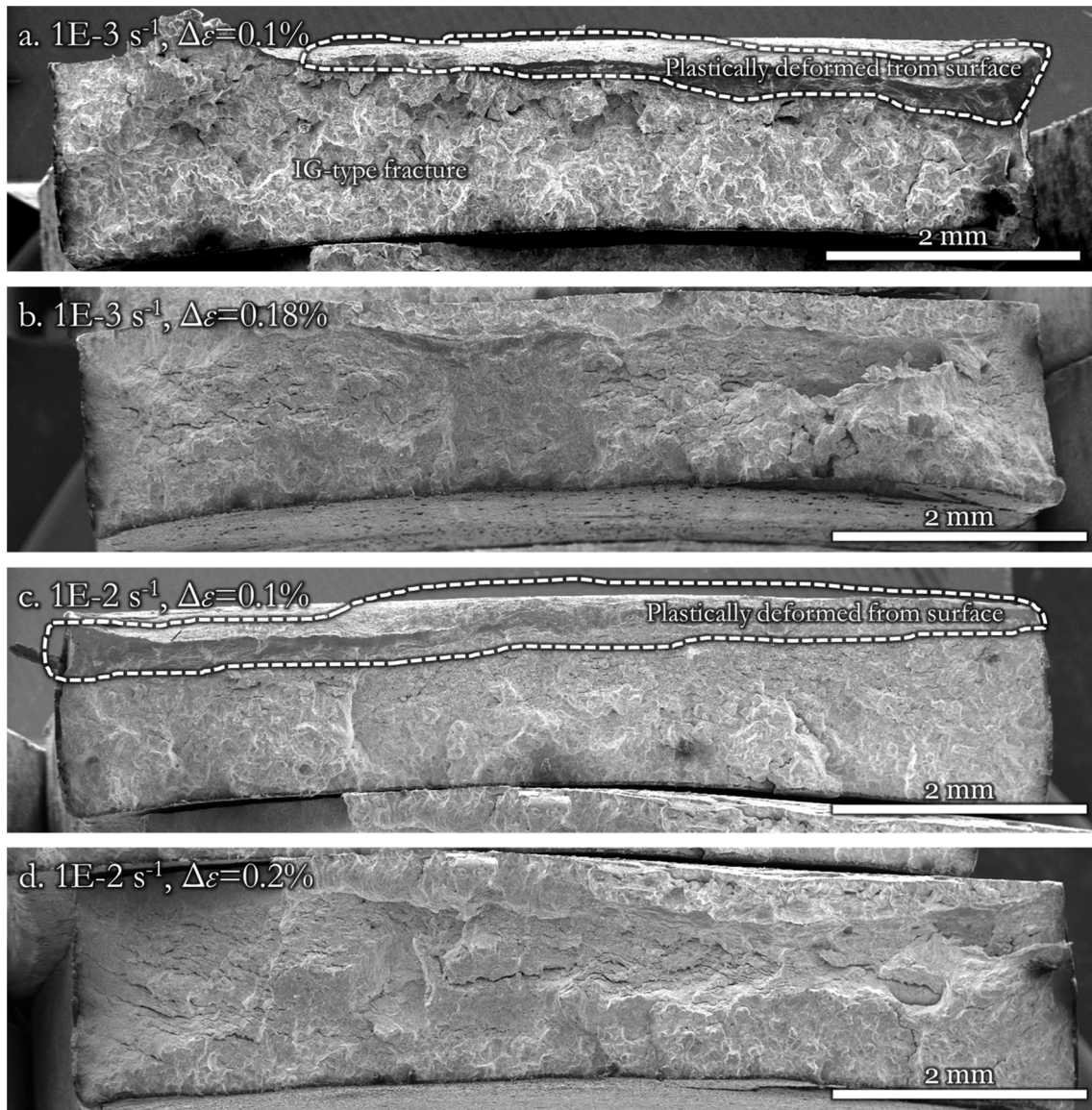
Fig. 22. Overview fractographs of the tested specimens. Nominal strain rates and global strain ranges are marked in each individual sub-figure.

with respect to α_v of the MI insulation layer [19]. Thus, to the layer A and B it was applied a temperature gap of $\Delta T = 30°C$ [19] and the duration of this loading step was chosen in order to obtain a longitudinal strain rate $\dot{\varepsilon}_{22}$ on the lead sheath equal to the strain rate measured during the experimental fatigue tests on the specimens.

In the end, during the cable production the layer E is winded tangentially with a positive tension, which causes a compression of the inner layers. This situation was simulated by means of a negative thermal gap on the steel tape of $\approx 20°C$, which allowed to obtain a positive preload of about 200 MPa on the layer E [19].

Since the damaging effect introduced by the notch factor is determined by a comparison between the fatigue curves of the real power cable with and without the geometrical irregularity, it was supposed that these are described by the Coffin-Manson-Basquin (CMB) equation (Equation 5) with the same slope parameters and different intercepts. Considering solicitations acting only in the lead plastic field, thus in the low cycle fatigue domain (LCF), the CMB equation becomes:

$$\varepsilon_{g,22} = A_{pl,s}(N_s)^{b_{pl}}; \varepsilon_{g,22} = A_{pl,i}(N_i)^{b_{pl}}$$

Where N_s is the number of cycles to failure for the model with a smooth lead layer and N_i has the same meaning for the model with the geometrical irregularity. Then, it can be written the percentage life of the cable with the geometrical irregularity with respect to the ideal condition:

$$\frac{\varepsilon_{g,22}}{\varepsilon_{g,22}} = \frac{A_{pl,s}}{A_{pl,i}} \cdot \left(\frac{N_s}{N_i}\right)^{b_{pl}} = k_f \cdot \left(\frac{N_s}{N_i}\right)^{b_{pl}} \rightarrow k_f = \left(\frac{N_i}{N_s}\right)^{b_{pl}}$$

$$\frac{N_i}{N_s} = k_f^{\frac{1}{b_{pl}}}$$

This situation consists in the limit case in which the lead sheathing is working in pure plastic conditions. The second limit case was found supposing that the same layer is subjected to solicitations acting only in its elastic field and a similar relation was found:

$$\frac{N_i}{N_s} = k_f^{\frac{1}{b_{el}}}$$

In this way, the real-life loss could be estimated considering a realistic working condition in between the two limit cases.

Being $k_f = 1 + q(k_\varepsilon - 1)$, the qualitative effect of the irregularity was studied by the computation of the strain concentration factor in the real configuration, recalling that the notch sensitivity (estimated in the
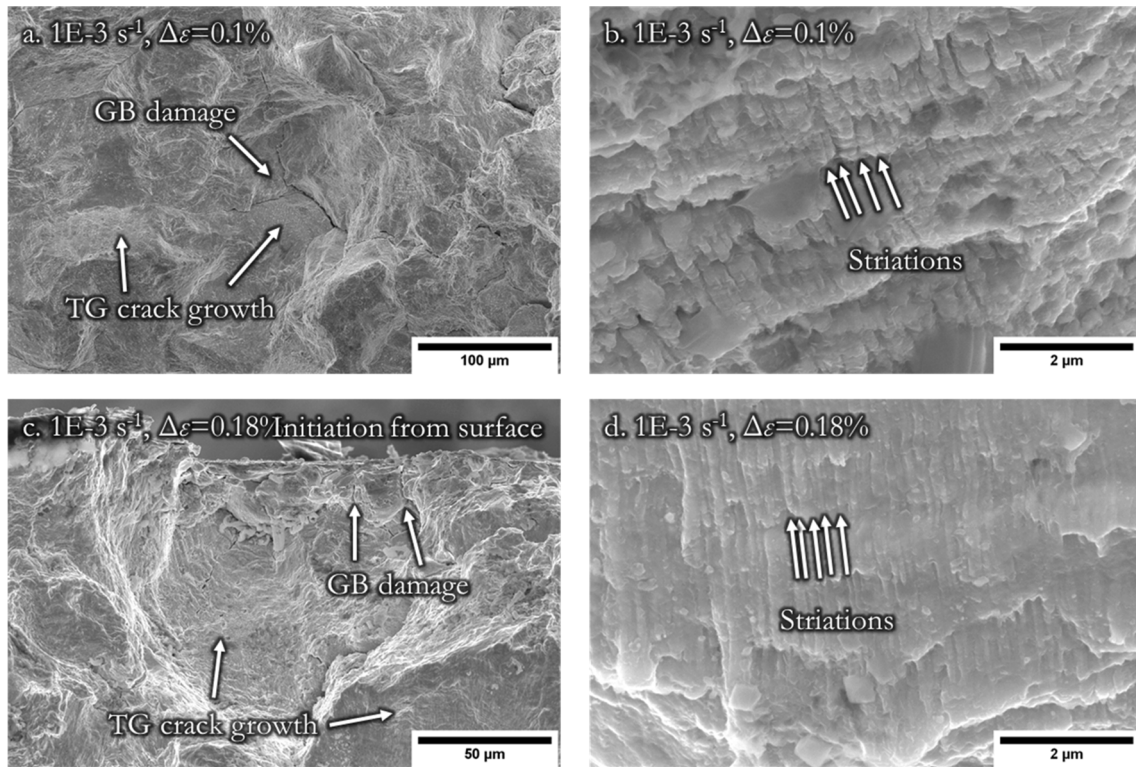
Fig. 23. Detailed fractographs of the specimen tested with nominal strain rate 1E-3 s^{-1}. a&b: global strain range of 0.1%; c&d: global strain range of 0.18%.
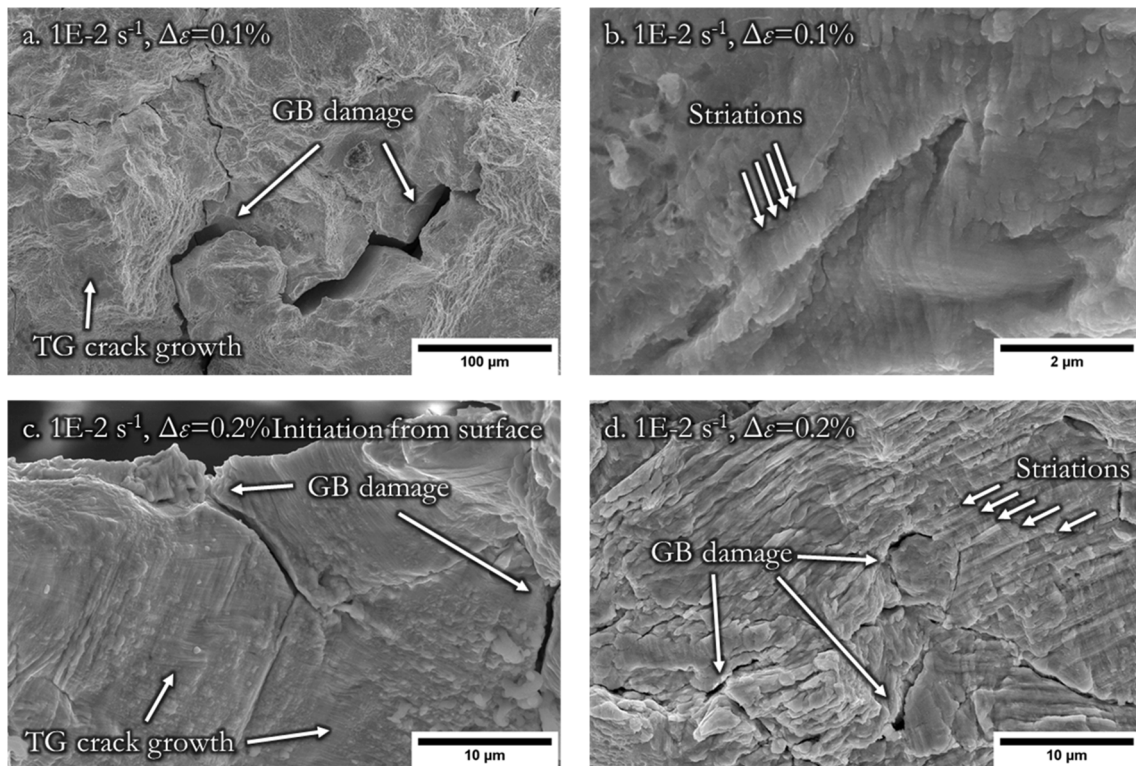
Fig. 24. Detailed fractographs of the specimen tested with nominal strain rate 1E-2 s^{-1}. a&b: global strain range of 0.1%; c&d: global strain range of 0.2%.

previous chapter for the conditions of interest) is a function of geometry, strain rate and temperature.

Finally, all the strain components of the most solicited point on the lead layer (Fig. 20) were selected as outputs to compute the Von Mises equivalent strain.

In a multiaxial stress and strain condition, the strain concentration factor definition is not univocal. Indeed, the usual formula for the strain concentration factor computation considers the maximum strain values

for the same global strain, which depends on the nature of the applied load. In this case, k_ε was computed considering the division of the maximum equivalent strain values at constant global strain along the longitudinal direction (y) $\varepsilon_{g.22}$:

$$k_\varepsilon = \left(\frac{\varepsilon_{max,eq,irr}}{\varepsilon_{max,eq,smo}} \right)_{|\varepsilon_{g.22}}$$

From the chart in Fig. 21 (analogous to the ones obtained during the study of the lead specimens) it was computed the trend of k_ε, which is almost constant along all the global strain field.

Its values for the two nominal strain rates are collected in Table 7, where also the values for the fatigue concentration factor were computed (Equation 3). There it is evident that the fatigue concentration factors are lower than the ones computed from the experimental analysis. This means that the irregularity has a lower damaging effect on the power cable than the expected one from the experimental fatigue tests.

In the end the percentage life loss for a lead layer working in between of its Low Cycle Fatigue domain and High Cycle Fatigue domain was computed and the results are collected in Table 8. Since the lead layer is working in a predominant plastic field, the life losses are for sure closer to a pure plastic load effect. For this reason, a non-dramatic life loss near can be expected, thus it can be concluded that the irregularity has a limited effect on the fatigue life of the power cable both in case of high and low cyclic deformations. Future investigations will be addressed to investigate the complete three-dimensional case focusing also on the thickness effect and induced modes [23–25].

6. Fractography

Fig. 22 shows the overview of the fractographies by scanning electron microscopy (SEM) from the failed specimens tested with two nominal strain rates (1E-2 s^{-1} and 1E-3 s^{-1}) and two global strain ranges (0.1% and 0.2%, i.e. the lowest and the highest). A common feature is that there seems no clear single damage initiation site for all the tested specimens. For the specimens tested with a lower strain range (0.1%), the surfaces seem to be plastically deformed (Fig. 22 a and c). On the contrary, the specimens tested at a higher strain range (0.18% and 0.2%) show a less plastic deformation close to the surfaces and a more brittle-like crack initiation and growth behavior (Fig. 22 b and d). For all four specimens, an intergranular type fracture can be noticed along with *trans*-granular features from the overview fractographies, indicating a tendency of grain boundary damage during failure. The slow strain rate seems to lead a higher fraction of intergranular features in comparison with the higher strain rate ones (e.g. Fig. 23a vs. Fig. 23c).

Figs. 23 and 24 show a closer look at the fractographic features in the tested specimens. Though grain boundary damage plays an important role, all specimens show clear *trans*-granular striations together with the intergranular fracture features. For the specimens tested at a higher strain range of both strain rates (0.18% and 0.2%, i.e. Figs. 23c and 24c), the specimen surfaces seem to show an initiation from grain boundary damages followed by *trans*-granular crack growth in the form of striations. Nevertheless, this damage initiation from surface does not seem to happen in a single site, but happens generally from multiple sites when referring to the overview fractographies in Fig. 22 b and d.

Considering the deformation and failure mechanisms, it is always a combined effect from both creep and fatigue in the tested specimens. But depending on the strain rate and range, the contribution can be a bit different between the cases. When testing at slower strain rates, the creep deformation contributes more due to a longer deformation time scale, and thus the damage gets accumulated more easily at grain boundaries and form grain boundary decohesion (e.g. Fig. 23a vs. Fig. 23c). When testing at a larger strain range, the heavier plastic deformation made the local stress level higher and thus the *trans*-granular crack growth more easily. These are in agreement with the previous results from both macro-scaled mechanical testing [12] and small-scale

in-situ testing [16] as well as the numerical analysis in the above sections. The interaction between creep and fatigue is a complex but important topic for developing a safe and knowledge-based prediction of the operational life of the components.

7. Conclusions

The notch fatigue sensitivity of a lead alloy is assessed in the case of blunt notches subjected to different strain rates at room temperature through testing, material model calibration and FEM analysis. The following conclusions on the influence of irregularities in full scale components is then modelled with FEM and on the fatigue life reduction due to the irregularities are drawn:

- Comparing the results of fatigue tests in global displacement control with and without the irregularities, a clear reduction on the global strain range is observed due to the presence of the defect.
- Due to plasticity, the strain concentration kε is not only a geometrical property, but depends on the strain level also. The irregularity causes a strain localization computed, in terms of effective Von Mises strain, as a strain concentration factor between 1.5 and 2.2 for both strain rates, with higher values associated to higher global strain range. No difference due to strain rate is detected in the range analysed.
- The notch sensitivity q depends on the global strain level and on the strain rate. As expected, a lower strain rate reduces the notch sensitivity. The values range from 0.7 to 0.25 in the range of strain and strain rates tested.
- A section of the full cable has been approximated using a simplified 2D axisymmetric mesh, imposing loading conditions of internal and longitudinal expansion due to temperature increase. The equivalent strain, computed with and without irregularities and then corrected with the notch strain sensitivity factor, indicates a reduction of fatigue life proportional to the strain rate and the strain level. The reduction is in the order of magnitude of a minimum of a few percentage points for high deformation (dominant plastic strain) to a maximum of around 20% for small deformations (dominant elastic strain).
- The main conclusion is that this type of irregularity, despite being undesirable, does not pose a significant threat to the structural integrity of the sheathing over its expected service life.
- The study on the notch sensitivity of the lead alloy should be extended to different geometries, strain rates and temperatures for a complete characterization.
- The fracture investigation evidenced how damage is the result of the interaction of fatigue and creep mechanisms, with the contemporary presence of intergranular and *trans*-granular fractures. The relative importance of one or the other damage mechanism depends on the strain rate, with a higher impact of creep deformation and grain boundary damage for lower strain rates.

Declaration of Competing Interest

The authors declare that they have no known competing financial interests or personal relationships that could have appeared to influence the work reported in this paper.

Acknowledgements

References

[1] Wu Z, Yang M, Zhao K. Fatigue Crack Initiation and Propagation at High Temperature of New-Generation Bearing Steel. Metals 2021;11:25.

[2] Yukio Takahashi. Creep-fatigue interaction: its mechanism and predictability. Asian Pacific Conference for Materials and Mechanics 2009 at Yokohama, Japan, November 13 2016.

[3] Moore, Herbert Fisher; Alleman, Norville James. The creep of lead and lead alloys used for cable sheathing, a report of an investigation conducted by the Engineering Experiment Station. University of Illinois, Engineering Experiment Station, Bulletin no. 243. 1932.

[4] Dollins, Curtis Walter; Betzer, Cecil E. Creep, fracture, and bending of lead and lead alloy cable sheathing. University of Illinois, Engineering Experiment Station, Bulletin no. 440. 1956.

[5] Feltham P. On the Mechanism of High-Temperature Creep in Metals with Special Reference to Polycrystalline Lead. Proc Phys Soc London, Sect B 1956;69(12): 1173–88.

[6] David Glyn Havard. Fatigue of lead cable-sheathing alloys. Ontario hydro research quarterly. 1972.

[7] P. Anelli, F. Donazzi, W.G. Lawson. The fatigue life of lead alloy E as a sheathing material for submarine power cables. IEEE Transactions on Power Delivery. Volume: 3, Issue: 1. 1988.

[8] Sahota MK, Riddington JR. Compressive creep properties of lead alloys. Mater Des 2000;21:159–67.

[9] Linul E, et al. Low-cycle fatigue behaviour of ductile closed-cell aluminium alloy foams. Fatigue Fract Eng Mater Struct 2017;40(4):597–604.

[10] Viespoli, Luigi Mario; Johanson, Audun; Alvaro, Antonio; Nyhus, Bård; Sommacal, Alberto; Berto, Filippo. (2018) Tensile characterization of a lead alloy: creep induced strain rate sensitivity. Materials Science & Engineering: A. vol. 744.

[11] Viespoli, Luigi Mario; Johanson, Audun; Alvaro, Antonio; Nyhus, Bård; Berto, Filippo. (2019) Room temperature creep mechanism of a Pb-Sn-Sb lead alloy. Procedia Structural Integrity. vol. 18.

[12] Luigi Mario Viespoli, Audun Johanson, Antonio Alvaro, Bård Nyhus, Filippo Berto, Subsea power cable sheathing: an investigation of lead fatigue performance, Procedia Structural Integrity, Volume 28, 2020.

[13] Johanson, Audun; Viespoli, Luigi Mario; Alvaro, Antonio; Berto, Filippo. (2019) Small and Full-Scale Fatigue Testing of Lead Cable Sheathing. ISOPE - International Offshore and Polar Engineering Conference. Proceedings.

[14] Johanson, Audun; Viespoli, Luigi Mario; Nyhus, Bård; Alvaro, Antonio; Berto, Filippo. (2018) Experimental and numerical investigation of strain distribution of notched lead fatigue test specimen. MATEC Web of Conferences. vol. 165:05003.

[15] Viespoli, Luigi Mario; Johanson, Audun; Alvaro, Antonio; Nyhus, Bård; Berto, Filippo. (2019) Strain controlled medium cycle fatigue of a notched Pb-Sn-Cd lead alloy. Engineering Failure Analysis. vol. 104.

[16] Di Wan, Luigi Mario Viespoli, Audun Johanson, Anette Brocks Hagen, Filippo Berto, Antonio Alvaro, Tensile and fatigue behavior of a Pb-Sn-Sb alloy investigated via small-scale in-situ mechanical testing in SEM, Procedia Structural Integrity, Volume 28, 2020.

[17] Huang ZY, Pilgrim JA, Lewin PL, Swingler SG, Tzemis G. Numerical thermo-mechanical stress analysis for HVDC Cables. Electrical Insulation Conference 2014.

[18] Huang ZY, Pilgrim JA, Lewin PL, Swingler SG, Payne D. Current rating methodology for mass impregnated HVDC cables. Electrical Insulation Conference (EIC) 2013.

[19] Viespoli Panza, Johanson Alvaro, Soma' Berto. Tape winding angle influence on subsea cable sheathing fatigue performance. Eng Struct 2020.

[20] Roesler J, et al. Mechanical Behaviour of Engineering Materials. Ceramics, Polymers and Composites, Springer: Metals; 2007.

[21] Bentachfine S, et al. Notch effect in low cycle fatigue, Elsevier. Int J Fatigue 1999;21.

[22] Diana FEA, https://dianafea.com/manuals/d944/Analys/node405.html.

[23] Berto F, Lazzarin P, Wang CH. Three-dimensional linear elastic distributions of stress and strain energy density ahead of V-shaped notches in plates of arbitrary thickness. Int. J. Fracture 2004;127(3):265–82. https://doi.org/10.1023/B: FRAC.0000036846.23180.4d.

[24] Berto F, Lazzarin P, Kotousov A. On higher order terms and out-of-plane singular mode. Mech Mater 2011;43(6):332–41. https://doi.org/10.1016/j.mechmat.2011.03.004.

[25] Pook LP, Campagnolo A, Berto F. Coupled fracture modes of discs and plates under anti-plane loading and a disc under in-plane shear loading. Fatigue Fract Eng Mater Struct 2016;39(8):924–38.